ACS ES&T Water

pubs.acs.org/estwater

Article

Binder-Free Fe (II) Sustained-Release Electrode for Enhanced Flow-Through Electro-Fenton Degradation on Aniline-Containing Wastewater

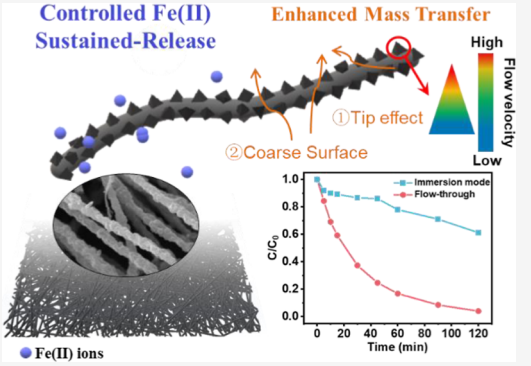
Jiamin Gao, Yujun Zhou,* Wei Zhang, Xuran Yang, Yiyuan Yao, Chengming Xiao, Xin Guo, Junwen Qi, Zhigao Zhu, Yue Yang, and Jiansheng Li*

Cite This: *ACS EST Water* 2024, 4, 4625−4635

Read Online

ACCESS | Metrics & More | Article Recommendations | Supporting Information

ABSTRACT: The ferrous-based (Fe(II)) electro-Fenton (EF) process for pollutant removal in wastewater has attracted great attention, while the unstable Fe(II) ion continuous supply and low mass transfer efficiency are vital challenges to hinder the pollutant degradation effects and further practical applications. Herein, we proposed an Fe(II) sustained-release anode coupled with a flow-through system to address this bottleneck problem. In our study, a binder-free Fe(II) sustained-release electrode was synthesized by the electrospinning method and employed in an EF reactor to treat aniline-containing wastewater. The high catalytic iron species was well dispersed and nanoconfined in nanofibers, which ensures a continuous supply of Fe(II) ions and enables a controlled homogeneous/heterogeneous coexistence environment, benefiting aqueous aniline removal efficiency (96.1% of aniline removed within 120 min). The rough surface of nanofibers and flow-through configuration greatly accelerate mass transfer kinetics (k = 0.027 min^{-1}, increased 6.5 times) since the contact chances between the targeted pollutants and the catalyst were mandatorily enhanced. The optimal conditions for aniline degradation were investigated. Four degradation pathways and probable mechanisms for aniline removal were proposed. CFD simulations were utilized to elucidate the fluid velocity distribution in the flow-through reactor. The work offers insights into constructing a rational EF system and developing a high-performance electrochemical technology for wastewater remediation.



KEYWORDS: *electro-Fenton, Fe(II) sustained release, nanofiber electrode, flow-through, mass transfer, aniline degradation*

INTRODUCTION

Electrochemical advanced oxidation processes have been regarded as a promising technology as the generated hydroxyl radical ($HO^{\bullet}$) is a highly reactive oxygen species (ROS) and capable of unselectively degrading most refractory pollutants in water.[1,2] Ferrous-based (Fe(II)) materials are the most widely applied catalysts which could activate H_2O_2 to generate $HO^{\bullet}$ through electro-Fenton (EF) reactions and be oxidized to ferric iron (Fe(III)).[3,4] The stable supply of Fe(II) in the system is crucial for enhancing the generation of ROS and keeping the EF reaction going.[5] The homogeneous Fenton reaction has a much higher catalytic efficiency than heterogeneous reactions. However, it had the difficulty of catalyst recovery, and large amounts of iron mud were produced. Developed heterogeneous reactions could relieve some of the problems, but the limited Fe(II) ions restrict the quantity of $HO^{\bullet}$ generation and greatly hinder the EF reaction performances.[6] Besides, the sluggish reaction kinetics resulting from the limited mass transfer in the EF system also adversely affects its ability to degrade pollutants.[7]

Among numerous Ferrous-based catalysts, iron-based metal−organic framework (MOF)-derived carbon is favored for its high specific surface area, plenty of active sites, and excellent catalytic ability.[8,9] Notably, MIL-MOFs constructed from trivalent metal centers and carboxylate-bridged ligands were of particular interest due to their approachable metal sites and relatively high chemical stability in the electrocatalytic field.[10,11] However, a decrease of the active area was often seen during pyrolysis because of the agglomeration of Fe particles and structural collapse, which led to the incomplete exposure of the active sites and poor catalytic abilities.[12] The electrospinning technique, which immobilizes and disperses the presynthesized MOF nanocrystals on the fibers, could ingeniously solve these problems.[13] The catalytic iron species

Received: July 24, 2024
Revised: September 19, 2024
Accepted: September 24, 2024
Published: October 2, 2024



Downloaded from pubs.acs.org/aewcaa/article-pdf/4/10/4625/4093023/ew4c00679.pdf by DOKUZ EYLUL UNIV user on 28 August 2026

© 2024 American Chemical Society

https://doi.org/10.1021/acsestwater.4c00679
ACS EST Water 2024, 4, 4625−4635

anchored on the fiber were separated in space, which avoids particle agglomeration and fully exposes the active sites.[14] More importantly, the binder-free electrodes prepared through the electrospinning method were supposed to have a controlled supply of Fe(II), enabling a homogeneous/heterogeneous coexistence environment boosting the EF reactions.

Apart from the sustained supply of Fe(II) ions, enhancing the mass transfer efficiency in the EF system for ROS effective generation and higher ROS utilization was also indispensable.[15] Most investigations were conducted in laboratory-scale immersion mode or flow-by reactors.[16] The electrochemical reaction in these modes usually occurs only at the electrode surface, resulting in low active site utilization and pollutant degradation efficiency.[17] Flow-through configurations provide a promising solution. Water flows vertically through the two parallel porous electrodes sequentially, and the electrical resistance is greatly reduced under this forced mass transfer. The extremely narrow space between the electrodes could increase the exposure of the targeted pollutants to more active sites.[18,19] Moreover, products generated at the former electrodes can act as reactants to the latter electrode along with the water flow, which may lead to a better performance of pollutant elimination.[20] Compared to immersion mode, the kinetics of pollutant degradation in flow-through reactors could improve by orders of magnitude and result in approximately 33% energy saving.[21]

Herein, we constructed an enhanced flow-through EF system using a binder-free Fe(II) sustained-release electrode derived from pyrolytically representative iron-based MIL-MOFs, MIL-101(Fe). Anchoring the iron species onto nanofiber channels could achieve its homogeneous distribution throughout the matrix, which brings out high catalytic performance and a stable Fe(II) source supply. The increased fiber surface roughness and resulting tip effect could increase the disturbance of water and enhance the mass transfer efficiency in this specific flow-through reactor. Aniline, which is a widespread industrial pollutant, was selected as a target pollutant and its degradation performance was investigated. Taking an immersion mode as a control, the feasibility of this enhanced flow-through EF system was verified. The degradation pathway of aniline was explored. And computational fluid dynamics (CFD) studies were conducted to further reveal the superiority of mass transfer and degradation in flow-through reactors. The current study provides new insights into the construction of a sustainable EF catalytic system with the potential for practical applications.

MATERIALS AND METHODS

Materials and Reagents. Graphite felt (thickness: 3 mm) was purchased from Beihai Carbon Co., Ltd. (Qingdao, China). Chemical reagents used in the experiments were all of analytical grade and purchased from Sinopharm (China), including ferric chloride hexahydrate ($FeCl_3{\cdot}6H_2O$), terephthalic acid (H_2BDC), *N*,*N*-dimethylformamide (DMF), polyacrylonitrile (PAN), sodium hydroxide (NaOH), sodium sulfate (Na_2SO_4), sulfuric acid (H_2SO_4), nitric acid (HNO_3), hydrochloric acid (HCl), hydrogen peroxide (H_2O_2), titanium oxalate ($C_4O_9Ti.2K$), 60% polytetrafluoroethylene (PTFE) suspension, dimethyl sulfoxide, 2,4-dinitrophenylhydrazine, 5,5-dimethyl-1-pyrroline *N*-oxide (DMPO), sodium nitrate ($NaNO_3$), sodium chloride (NaCl), sodium hydrogen carbonate ($NaHCO_3$), and humic acid (HA). Ultrapure water (Miaozhiyi, China) with a resistivity of 18.25 MΩ cm was used in experiments.

Synthesis of MIL-101 (Fe) Powders. In a typical synthesis process, 0.675 g of $FeCl_3{\cdot}6H_2O$ and 0.206 g of H_2BDC were dissolved in 15 mL of DMF. After being stirred thoroughly for 20 min, the mixed solution was transferred into a 50 mL Teflon-lined autoclave and heated at 110 °C for 20 h. After cooling to room temperature, the product was centrifuged to obtain a light-orange precipitate, which was washed with DMF and ethanol three times. Finally, the solid products were dried at 80 °C for 6 h to obtain MIL-101 (Fe).

Synthesis of MIL-101 (Fe)-PAN. Typically, 0.6 g of MIL-101 (Fe) powder was dissolved in 6 mL of DMF with sonication until it was fully dispersed. Subsequently, 0.8 g of PAN was added into the solution and stirred at 65 °C for 4 h to obtain the electrospinning precursor. The electrospinning process was carried out by applying a high positive voltage (12.0 kV) at a collection distance of 15 cm. The injection speed was fixed at 0.08 mm min^{-1}. The finally obtained nanofibers were naturally air-dried and denoted as MIL-101 (Fe)-PAN.

Synthesis of Fe-CNFs. The as-prepared MIL-101 (Fe)-PAN was placed in a tube furnace and heated to 260 °C for 2 h with a heating rate of 1 °C min^{-1} under a N_2 atmosphere. Then the temperature was subsequently increased to 800 °C for 5 h with a heating rate of 3 °C min^{-1}. The obtained carbonized nanofiber was named Fe-CNF-8. When the temperature was increased to 700, 900, and 1000 °C, the corresponding obtained Fe-CNFs were named Fe-CNF-7, Fe-CNF-9, and Fe-CNF-10, respectively. The Fe-CNF production process is shown in Figure S1.

Preparation of Modified Graphite Felt. The graphite felts were washed in an ultrasonic bath with HNO_3 (3 mol L^{-1}), acetone, and deionized (DI) water, respectively, in sequence for 30 min and dried at 80 °C. 0.4 g of carbon black, 0.7 mL of PTFE, 0.8 mL of DI water, and 2.8 mL of ethanol were mixed to form a highly homogeneous coating, which was uniformly coated onto a 5*5 cm graphite felt. Subsequently, the graphite felt was heated to 360 °C in a muffle furnace at a heating rate of 12 °C min^{-1} and held for 30 min to obtain the modified graphite felt.

EF Pollutant Degradation Experiments. The pollutant degradation experiments were carried out in a flow-through EF reactor (Figure S2). The Fe-CNF self-supported electrodes and modified graphite-felt cathode were utilized as the anode and cathode, respectively. A 25*25 mm platinum mesh was used as a current collector. The cathode and the anode were separated by an isolation layer, and a silicone spacer was utilized to prevent reactor leakage. 80 mL of aniline (20 mg L^{-1}) containing 50 mM Na_2SO_4 was used as the target contaminant. The degradation process was carried out in upflow water inlet, in recirculating filtration mode. The solution was exposed to oxygen during the reaction. The impact of the solution's initial pH (3−7), flow rate (2−20 mL min^{-1}), and applied voltage (1.8−2.8 V) on aniline degradation kinetics were investigated. The solution's initial pH was adjusted with 1 M H_2SO_4 or NaOH. The applied voltage was controlled by an adjustable DC-regulated power supply (HSPY-120−01). At intervals, 0.75 mL of the sample was taken and transferred to a 2 mL centrifuge tube containing 0.75 mL of methanol for HPLC analysis.

Electrochemistry Measurements. Cyclic voltammetry (CV) and electrochemical impedance spectroscopy (EIS)

Downloaded from pubs.acs.org/aewcaa/article-pdf/4/10/4625/4093023/ew4c00679.pdf by DOKUZ EYLUL UNIV user on 28 August 2026

https://doi.org/10.1021/acsestwater.4c00679
ACS EST Water 2024, 4, 4625−4635

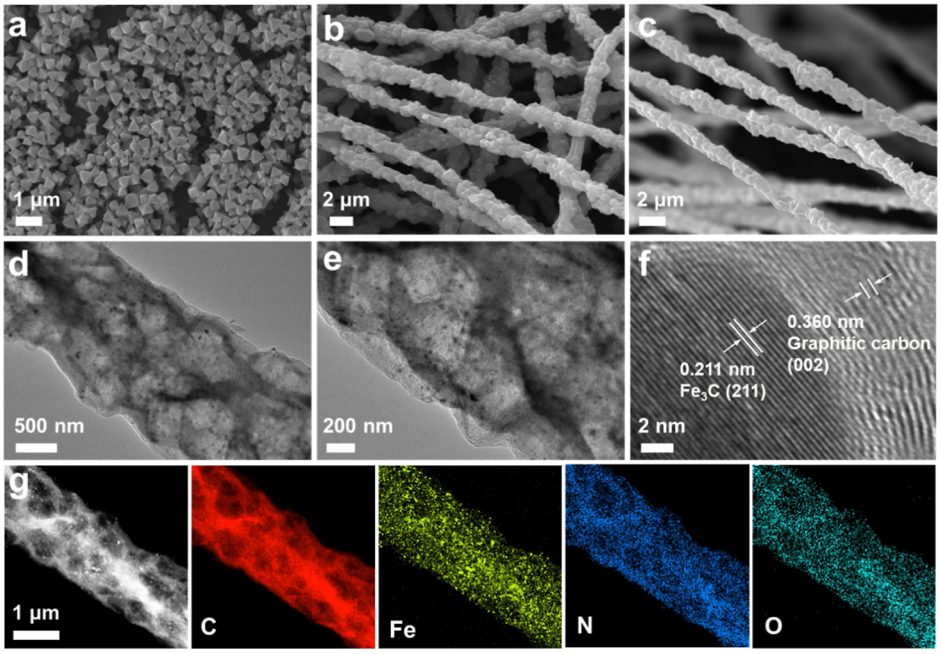


Figure 1. SEM images of (a) MIL-101 (Fe), (b) MIL-101 (Fe)-PAN, and (c) Fe-CNF-8; (d,e) TEM, (f) HRTEM, and (g) EDS elemental mapping of Fe-CNF-8.

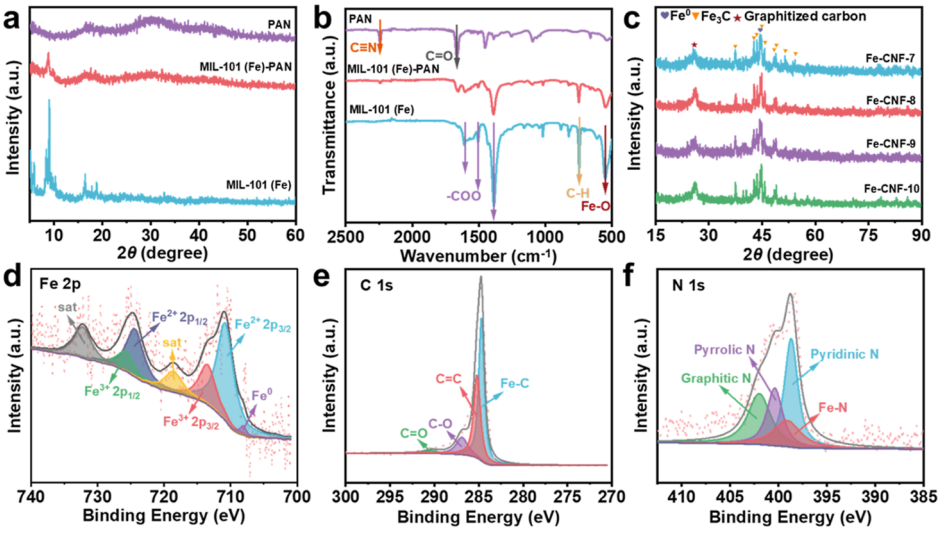


Figure 2. (a) XRD patterns and (b) FT-IR spectra of MIL-101 (Fe), MIL-101 (Fe)-PAN, and PAN; (c) XRD patterns of Fe-CNFs; (d) Fe 2p, (e) C 1s, and (f) N 1s in Fe-CNF-8.

measurements were performed by using an electrochemical workstation (CHI 760D). The CV experiment was conducted at a scan rate of 50 mV s^{-1} with low and high voltages of 1 and −1 V, respectively. During EIS measurements, the frequency used was from 100,000 to 0.01 Hz. All electrochemical tests were performed using a three-electrode system consisting of a working electrode (preparation material), a counter electrode (platinum plate), and a reference electrode (Ag/AgCl), and the electrolyte was a 50 mmol L^{-1} Na_2SO_4 solution.

Characterization. The structure and morphology of samples were confirmed by scanning electron microscopy (SEM, JEOL JSM 7800F) and transmission electron microscopy (TEM, FEI Tecnai 20 electron microscope). The crystal configuration and composition were evaluated by Bruker D8 at 40 kV and 40 mA by X-ray diffraction (XRD, Cu Kα, λ = 1.5418 Å). The N_2 adsorption and desorption isotherms were obtained from a Micromeritics ASAP-2020 instrument. The specific surface area was acquired by the Brunauer−Emmett−Teller (BET) method. The elemental composition was analyzed by X-ray photoelectron spectroscopy (XPS, PHI Quantera II ESCA system with Al Kα radiation at 1486.8 V). Fourier transform infrared (FT-IR) spectroscopy analysis was carried out using a Nicolet iS10 FT-IR spectrometer with a frequency range of 4000−500 cm^{-1}. Raman spectroscopy was conducted on a RENISHAW inVia reflex spectrometer system. The radical signals were collected by electron paramagnetic resonance (EPR) experiments (Bruker EMX 10/12).

https://doi.org/10.1021/acsestwater.4c00679
ACS EST Water 2024, 4, 4625−4635

Downloaded from pubs.acs.org/aewcaa/article-pdf/4/10/4625/4093023/ew4c00679.pdf by DOKUZ EYLUL UNIV user on 28 August 2026

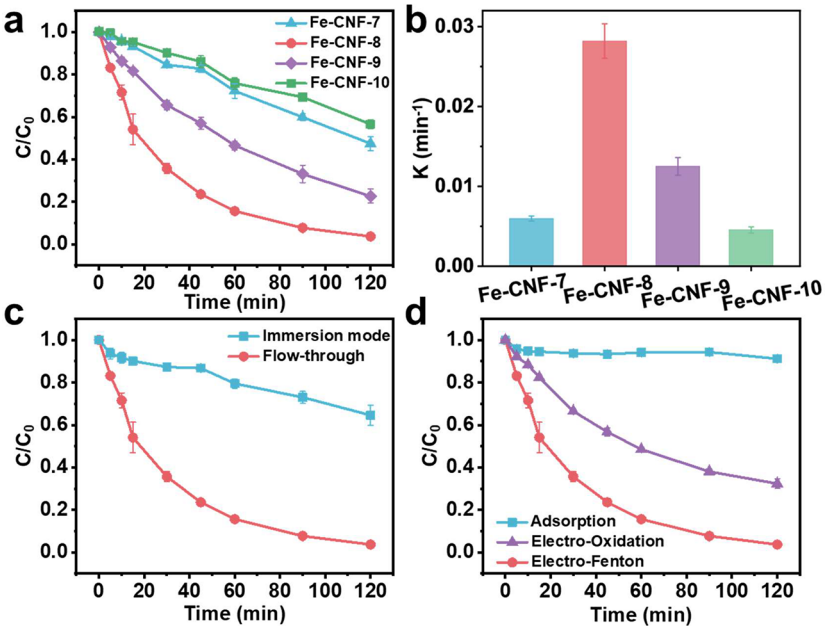


Figure 3. (a) Aniline removal efficiency of Fe-CNFs at different annealing temperatures; (b) corresponding pseudo-first-order rate constant of aniline for Fe-CNFs; (c) EF degradation efficiency comparison between flow-through and immersion modes; (d) comparison of aniline removal by different processes. Initial conditions: aniline, 20.0 mg L^{-1}; pH, 3; catalyst, 0.25 g L^{-1}; voltage, 2.6 V; Na_2SO_4 50 mmol L^{-1}.

RESULTS AND DISCUSSION

Characterizations of the Obtained Fe Sustained-Release Electrode. The surface morphology of the as-synthesized samples was observed by SEM and TEM. As shown in Figure 1a, the MIL-101 (Fe) powders demonstrated a regular and uniform octahedral morphology with an average size of 400−500 nm. The pristine PAN fibers exhibited an interlaced structure with a smooth surface with a uniform diameter of around 0.6 μm (Figure S3). After electrospinning, MIL-101 (Fe) nanocrystals were densely anchored on the PAN fibers (Figure 1b). The fibers became coarser in diameter (1.2 μm) due to the roughened surface. After carbonization at 800 °C, Fe-CNF-8 could still maintain the octahedral morphology of MIL-101 (Fe) (Figure 1c). The pyrolysis process resulted in a good dispersion of small Fe particles with an average size of 40 nm strung along the PAN-derived carbon fibers (Figure 1d,e), leading to the exposure of more active sites. Notably, Fe-CNF-8 possessed a core−shell structure with Fe_3C nanoparticles encapsulated by a graphitic carbon layer. The high-resolution TEM (HRTEM) image in Figure 1f showed a lattice fringe of 0.211 and 0.360 nm, which corresponded to the (211) and (002) planes of Fe_3C[22] and graphitic carbon,[23] respectively. The scanning TEM image and corresponding elemental map (Figure 1e) further revealed that N and O elements were uniformly distributed throughout the whole porous carbon matrix. Instead, Fe species were encapsulated within porous carbon. Other Fe-CNFs at different carbonization temperatures also showed similar nanofibrous structures as Fe-CNF-8 (Figure S4). Compared with Fe-CNF-8, Fe-CNF-7 (Figure S5a) had no obvious Fe species. With the increase of pyrolysis temperature, both Fe-CNF-9 (Figure S5b) and Fe-CNF-10 (Figure S5c) exposed large Fe particles and tended to aggregate. Moreover, the Fe content of Fe-CNFs was determined by ICP-OES (Table S1), Fe-CNF-8 had a relatively high Fe content, and the high and well-dispersed Fe content may contribute to its EF degradation performance. All the observations confirmed the successful synthesis of Fe-CNFs.

To give an in-depth insight into the composition, XRD and FT-IR analyses were carried out. As shown in Figure 2a, the characteristic peaks of MIL-101 (Fe) were well matched with the simulated diffraction patterns of the MIL-101 single-crystal structure data.[24] The same characteristic peaks were observed in MIL-101(Fe)-PAN, whereas there were no obvious characteristic peaks in PAN. From the FT-IR spectra (Figure 2b), the absorption peaks at 1602, 1504, and 1391 cm^{-1} were ascribed to the −COOH groups.[23] The C−H bending vibrational absorption peak of the benzene ring was located at 750 cm^{-1}.[25] The absorption peak at 550 cm^{-1} was attributed to the stretching of the Fe−O bond.[26] A distinct peak of PAN appeared at 2242 and 1632 cm^{-1} attributed to the −C≡N group and −C═O group, respectively.[27] These results further demonstrated the successful fixation of MIL-101 (Fe) on the PAN fibers. As demonstrated in Figure 2c, after the pyrolysis process, the Fe-CNFs exhibit the same diffraction peaks. The peaks at 44.7° correspond to the (110) reflections of α-Fe (JCPDS no. 87-0722). Moreover, the peaks at 37.8, 42.9, 43.8, 45, 45.9, and 49.1° could be indexed to the (210), (211), (102), (031), (112), and (221) crystal planes of Fe_3C (JCPDS no. 35-0772), respectively. Additionally, the peak at 25.8° was attributed to the (002) crystal face of graphite carbon.

Raman spectroscopy was used to evaluate the degree of graphitization of carbon in the catalysts. The peaks at 1350 and 1590 cm^{-1} are the D and G peaks of carbon (Figure S6), which represent the degree of carbon defects and graphitization, correspondingly.[28] The calculated I_D/I_G values of Fe-CNF-7, 8, 9, and 10 were 1.10, 1.06, 1.13, and 1.24, respectively. The degree of graphitization showed a tendency to decrease and then increase with the increase of the carbonization temperature. The graphitization degree of Fe-CNF-8 is the highest, which indicates that moderate carbonization temperatures could contribute to the formation of well-graphitized carbon.[29] The specific surface area and pore structure of these catalysts

https://doi.org/10.1021/acsestwater.4c00679
ACS EST Water 2024, 4, 4625−4635

Downloaded from pubs.acs.org/aewcaa/article-pdf/4/10/4625/4093023/ew4c00679.pdf by DOKUZ EYLUL UNIV user on 28 August 2026

were characterized by a nitrogen adsorption/desorption instrument. As shown in Figure S7, the nitrogen adsorption and desorption curves were better in accordance with the IUPAC-IV type with a good mesoporous structure. The BET surface area and pore volume of Fe-CNFs increased from 197.5 $m^2\ g^{-1}$ (0.05 $cm^3\ g^{-1}$) to 296.8 $m^2\ g^{-1}$ (0.09 $cm^3\ g^{-1}$) as the carbonization temperature rose from 700 to 900 °C (Table S2). After further increasing the temperature, the specific surface area and pore volume of Fe-CNF-10 decreased significantly to 83.0 $m^2\ g^{-1}$ (0.04 $cm^3\ g^{-1}$). It is suggested that the appropriate carbonation temperature was conducive to the enhancement of the specific surface area and pore volume of the catalyst, exposing more active sites and thus providing more flow paths for the aqueous solution, which further promotes the possibility of reaction collisions and facilitates mass transfer.

The XPS survey spectrum in Figure S8a confirmed the existence of Fe, O, C, and N elements in Fe-CNFs. Meanwhile, the Fe 2p spectrum of Fe-CNF-8 (Figure 2d) displayed two peaks of Fe $2p_{3/2}$ and $2p_{1/2}$. Interestingly, the Fe $2p_{3/2}$ peak could be divided into three peaks at 708.1, 710.8, and 713.5 eV, corresponding to the characteristic binding energies of Fe (0), Fe (II), and Fe (III), respectively.[30] Figure S8b−d also demonstrates this result, except that Fe (0) is less abundant at lower carbonization temperatures. The weak signal of Fe indicated that Fe species were encapsulated within the carbon layer.[31] Figure 2e shows deconvolutions from C 1s spectra of Fe-CNF-8, where C 1s was fitted to four peaks at 284.7, 285.2, 286.9, and 290.3 eV, assigned to Fe−C, C═C, C−O, and C═C, respectively.[22] The N 1s high-resolution spectra (Figure 2f) could be deconvoluted into four characteristic peaks, corresponding to Fe−N (399.1 eV), pyridinic N (398.7 eV), pyrrolic N (400.4 eV), and graphitic N (402.0 eV).[10] The introduction of N enhanced the conductivity and stability of the electrode materials.[32]

Electrochemical Aniline Degradation. Figure S9 reveals the generation of H_2O_2 from the modified graphite felt via $2e^-$ ORR. The concentration of H_2O_2 accumulated with time. At 120 min, the H_2O_2 production gradually became larger from 6 to 38 mg L^{-1} with increasing operating voltage (1.8−2.6 V). A further increase of the voltage to 2.8 V resulted in a significant decrease of H_2O_2 production to 15 mg L^{-1}. This was probably due to the presence of other by-reactions at higher voltages, which in turn affected the selectivity of H_2O_2.[33]

The electrocatalytic performance of Fe-CNF electrodes in the EF system was assessed. As shown in Figure 3a, the electrocatalytic performance of Fe-CNFs showed a tendency to become better and then worse with increasing carbonization temperature. The highest catalytic performance was obtained with Fe-CNF-8, which could remove 96.1% of aniline within 120 min. Figure 3b compares their catalytic behavior more clearly by fitting the first-order kinetic reactions of aniline degradation. Fe-CNF-8 showed a maximum rate constant (k = 0.027 min^{-1}), which was about 4.7, 2.1, and 5.6 times higher than those of Fe-CNF-7, Fe-CNF-9, and Fe-CNF-10, respectively. As shown in Figure S10, the removal of aniline by CNF-8 was only 10%. The significant improvement in the performance of Fe-CNF-8 suggests that the regulation of carbonization temperature plays a critical role.[34]

With the aim of visually elucidating the advantages of the flow-through model equipped with an Fe-CNF electrode, two different systems consisting of the flow-through and regular immersion models were evaluated. Figure 3c shows the variation of aniline concentration with reaction time for different reactor configurations. Over 120 min of treatment, the removal of aniline was 96.1% in the flow-through system compared to 38.9% in the regular immersion model. Additionally, the value of k (0.027 min^{-1}) in the flow-through system increased dramatically, compared to the regular immersion model (0.0036 min^{-1}), suggesting tremendous advantages of the construction of the Fe-CNF-8 electrode material in this flow-through system. Comparisons were conducted with other procedures for aniline degradation, and the results are shown in Table S3. The substantial improvement of catalytic performance was ascribed to the enhanced mass transfer of aniline molecules to the catalytically active sites of the electrode by forced mass transfer within the flow-through system, whereas the regular immersion model relied on a slow diffusion process of the substance.[35]

The contribution of various reactions involved in the electrochemical advanced oxidation system,[36] such as adsorption, EF, and electrochemical oxidation, was further tested for the degradation of aniline. In Figure 3d, it is evident that adsorption contributes less to the reaction, with only 10.0% degradation efficiency. On the contrary, the electrochemical oxidation and EF processes showed 69.3% and 96.1% degradation efficiencies for aniline within 120 min, respectively. Therefore, the effective degradation of aniline was promoted by the synergistic effect of electrochemical oxidation and EF techniques.

Optimization of Operating Conditions for the Flow-Through EF Reactor. The effect of initial pH on degradation kinetics was investigated under similar conditions (Figure S11a,b). The highest aniline degradation efficiency of 96.1% was observed at pH 3, with a k value of 0.027 min^{-1}. In contrast, a slight decrease in degradation efficiency was observed at neutral and aniline natural pH 6 conditions. Similarly, the TOC removal decreased from 40.6% at pH 3 to 29.6% at pH 6 and 31.6% at pH 7. It is known that H_2O_2 is more stable under acidic conditions, thus facilitating the Fenton reaction.[7] Nevertheless, aniline was effectively degraded by the electrochemical system over a wide pH range. This solved the problem of the narrow pH range of the traditional Fenton process and the inevitable higher generation of iron sludge.

The flow rate determined the residence time of the pollutant molecules and therefore could have a significant effect on the removal efficiency of aniline. When the flow rate was increased from 2 to 10 mL min^{-1}, the aniline degradation efficiency increased from 53.3 to 97.1% with k increasing from 0.059 to 0.029 min^{-1} (Figure S11c,d). This might be due to the higher flow rates promoting mass transfer, shortening the time for contaminants to diffuse to the electrode surface, and increasing the number of cycles of pumped contaminants. After further increasing the flow rate to 20 mL min^{-1}, the degradation efficiency decreased to 94.9%. Because of the low retention time of the pollutant, there was a short contact time with the electrode.

The aniline degradation performance was then investigated as a function of the applied voltage. Enhanced degradation kinetics of aniline was recorded as the voltage decreased from −1.8 to −2.6 V under a flow rate of 5 mL min^{-1} (Figure S11e,f). The aniline degradation efficiencies were 45.4%, 58.0%, and 96.1%, respectively, with corresponding k values of 0.0048, 0.0071, and 0.027 min^{-1}. This was in anticipation, given that as the applied voltage was lower to −2.6 V, more

Downloaded from pubs.acs.org/aewcaa/article-pdf/4/10/4625/4093023/ew4c00679.pdf by DOKUZ EYLUL UNIV user on 28 August 2026

https://doi.org/10.1021/acsestwater.4c00679
ACS EST Water 2024, 4, 4625−4635

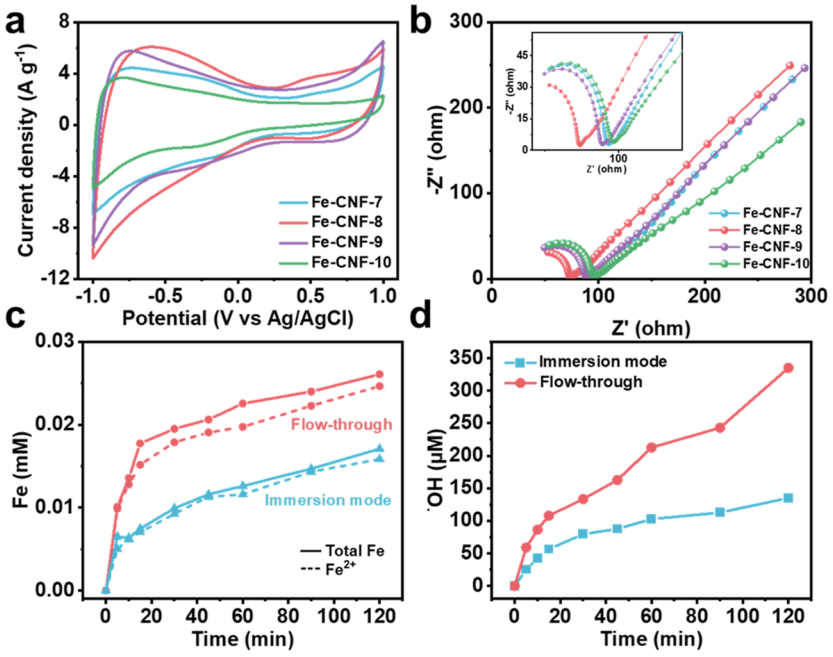


Figure 4. (a) CV curves (50 mV s^{-1}); (b) EIS curves. (c) Fe^{2+} and total iron concentration; (d) generated $HO^{\bullet}$. Initial conditions: aniline, 20.0 mg L^{-1}; pH, 3; catalyst, 0.25 g L^{-1}; voltage, 2.6 V; Na_2SO_4 50 mmol L^{-1}.

H_2O_2 was produced, which, in turn, yielded more $HO^{\bullet}$ for aniline degradation. However, the aniline degradation efficiency was lower when the voltage was further reduced to −2.8 V, which was consistent with the results of H_2O_2 production in Figure S9, probably due to the occurrence of other competing reactions such as excess H_2O_2 reacting with $HO^{\bullet}$ or H_2 production.[37]

Normally, there are numerous ions and natural organic matter in the actual aqueous bodies, which affect the catalytic performance by capturing free radicals, occupying catalyst sites, affecting the initial pH values, etc.[13] Therefore, the influences of typical anions (Cl^-, NO_3^-, and HCO_3^-) and natural organic matter HAs on the degradation of aniline were examined (Figure S11g,h). It was seen that NO_3^-, HCO_3^-, and HA all showed inhibitory effects on aniline removal. The effect of HCO_3^- was the most significant, in the presence of which the removal efficiency of aniline was reduced to 55.4%, and the efficiency of k also decreased from 0.027 to 0.0073 min^{-1}. This might be attributed to the formation of a hydroxide insulating film on the surface of iron by CO_3^{2-}formed from HCO_3^-, thereby restraining the catalytic activity of iron.[38] In addition, the degradation rate of aniline also decreased to 0.020 and 0.013 min^{-1} in the existence of NO_3^- and HA, respectively, which may be due to NO_3^- capturing $HO^{\bullet}$ to form $NO_3\cdot$ with weak oxidative capacity. Meanwhile, HA would compete with the target pollutant on the catalyst surface. On the contrary, the degradation of aniline was prominently promoted when Cl^- was present, where k increased from 0.027 to 0.035 min^{-1}. The oxidation process of aniline may be promoted by the formation of reactive chlorine species due to the oxidation of Cl^- at the anode.[39]

System Durability Evaluation. The recoverability and reusability of the catalyst are key factors for practical applications. Compared with conventional EF electrode materials, the self-supporting properties of the electrodes provide great convenience for reuse.[40] The durability of Fe-CNF-8 in the flow-through EF system was verified by reusing it (Figure S12). After three consecutive cycles, the degradation efficiency of aniline was maintained at more than 90%. The degradation efficiency of aniline was 69.8% after five consecutive cycles. This indirectly confirmed that the slow-release process of Fe was effective in enabling a continuous Fenton process.

Furthermore, the morphology of Fe-CNF-8 after reuse was investigated by SEM. Figure S13 shows that there was no prominent change in the surface morphology of Fe-CNF-8 after aniline degradation. However, the weakening of Fe signals in XRD and XPS indicated the release of Fe species, which was involved in the reaction during degradation, whereas the Fe 2p spectra showed a decrease in the content of Fe^{2+} and an increase of Fe^{3+} after reuse (Figure S14). Nevertheless, the crystal structure of Fe-CNF-8 was maintained after aniline degradation. We considered the described Fe-CNF-8 self-supporting electrode to be the more robust material for convenient reuse and is well suited for flow-through EF applications.

Mechanistic Formation and Determination of ROS. To further demonstrate the variation in electrode electrocatalytic performance, the electrochemical properties and behavior of the Fe-CNFs were evaluated. As illustrated in Figure 4a, the Fe-CNF-8 electrode had the largest integrated area of the CV curve among all the samples, which indicated that it has a superior electrochemical active area. The specific capacitance of the electrode materials was further calculated with the results shown in Table S4. The specific capacitance of Fe-CNF-8 was 68.67 F g^{-1}, which was larger than those of Fe-CNF-7 (51.38 F g^{-1}), Fe-CNF-9 (64.06 F g^{-1}), and Fe-CNF-10 (33.74 F g^{-1}). The ionic reaction kinetics of the electrode was further evaluated by EIS. Figure S15 provides a diagram of the equivalent circuit. The Nyquist plots in Figure 4b showed that Fe-CNF-8 possessed a minimum bulk resistance (R_s). In addition, the charge transfer resistances (R_{ct}) of Fe-CNF-7, 8, 9, and 10 were 87.94, 62.08, 82.86, and 94.81 Ω, respectively, after equivalent circuit fitting (Table S4). The smallest R_s and

Downloaded from pubs.acs.org/aewcaa/article-pdf/4/10/4625/4093023/ew4c00679.pdf by DOKUZ EYLUL UNIV user on 28 August 2026

https://doi.org/10.1021/acsestwater.4c00679
ACS EST Water 2024, 4, 4625−4635

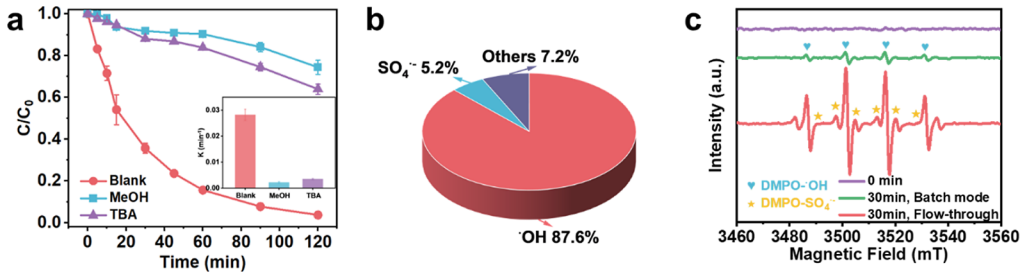


Figure 5. (a) Effect of radical scavengers on the aniline degradation process in the Fe-CNF-8/EF system; (b) contribution of different free radicals. (c) EPR spectrum of ·OH and $SO_4^{\bullet-}$ on Fe-CNF-8. Reaction conditions: aniline, 20.0 mg L^{-1}; initial pH, 3; catalyst, 0.25 g L^{-1}; voltage, 2.6 V; Na_2SO_4 50 mmol L^{-1}; DMPO 0.1 mol L^{-1}.

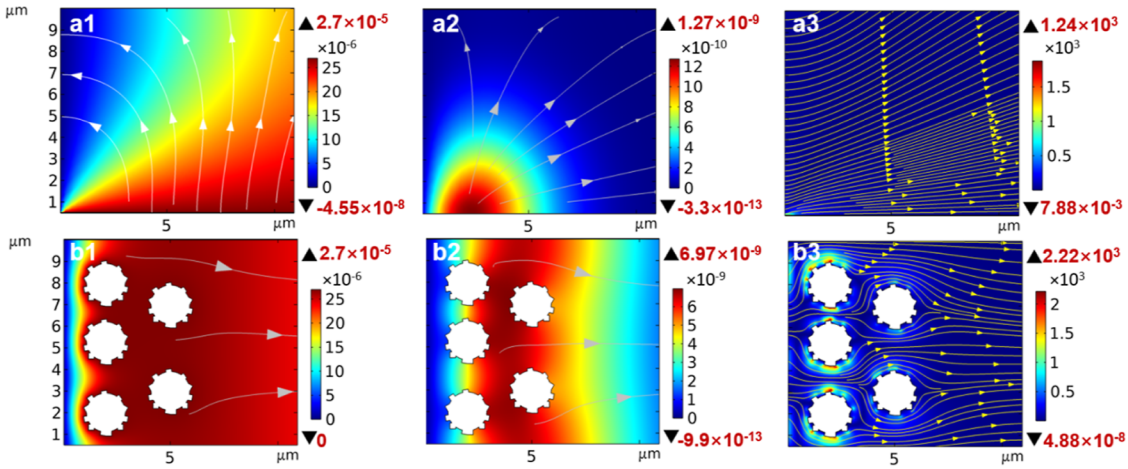


Figure 6. CFD simulations of the concentration of Fe^{2+} in the immersion mode (a1) and flow-through configuration (b1), concentration of $HO^{\bullet}$ in the immersion mode (a2) and flow-through configuration (b2), and fluid trajectory distributions in the immersion mode (a3) and flow-through configuration (b3).

R_{ct} were obtained for Fe-CNF-8, which indicated its high conductivity. The Warburg coefficients can be obtained from the slope of the curve of the real part (Z') of the complex impedance in the low-frequency region versus $\omega^{-1/2}$ (ω is the corner frequency). As shown in Figure S16, the fitting results revealed that Fe-CNF-8 had the lowest slope (σ = 5.92), which was about 0.055, 0.12, and 0.026 times that of Fe-CNF-7 (σ = 107.36), Fe-CNF-9 (σ = 50.57), and Fe-CNF-10 (σ = 230.68), respectively. It was proven that the Fe-CNF-8 electrode has the fastest ion transport rate. The superior electrocatalytic performance of Fe-CNF-8 compared with other electrodes may be attributed to its high electrochemical activity, high electrical conductivity, and fast ionic transport rate as well as its high content of well-dispersed Fe species, thus facilitating the degradation process of aniline.

As is well known, the degradation of pollutants by the EF process depends essentially on the formation of $HO^{\bullet}$ in solution, which is simultaneously affected by the concentration of Fe^{2+}. Therefore, changes in total iron and Fe^{2+} and $HO^{\bullet}$ concentrations were monitored in both systems. As shown in Figure 4c, the concentration of total iron in the flow-through reaction system increased rapidly to 0.02 mM in the first 30 min and then increased slowly and stabilized to 0.026 mM in 120 min. Notably, the Fe^{2+} concentration was 0.025 mM at 120 min, indicating that there was no excess Fe^{3+} in the system as Fe^{3+} could be reduced at the cathode to Fe^{2+} which could conduct the Fenton reaction. However, in the regular immersion model, although the trends of total iron and Fe^{2+} concentrations were similar to those of the flow-through system, the concentrations of total iron and Fe^{2+} were only 0.017 and 0.016 mM at 120 min, respectively, which were both significantly lower than those of the flow-through system. The cumulative $HO^{\bullet}$ concentration produced in the different systems further demonstrated the advantages of the flow-through EF system in the removal of aniline. After 120 min of reaction, the $HO^{\bullet}$ concentration generated by the flow-through system and the regular immersion model reached 135.0 and 335.1 μM, respectively, and showed a sharp increase in the flow-through system (Figure 4d). All of these results directly proved that the degradation of aniline was effectively enhanced by the flow-through system through the change in the configuration of the EF reactor, which was capable of generating more Fe^{2+} during the reaction process and forming $HO^{\bullet}$ faster to degrade the pollutant.

Free radical quenching experiments were carried out to further identify the active substances in the electrochemical oxidation system. Methanol was selected as a scavenger for $HO^{\bullet}$ and $SO_4^{\bullet-}$, while tertiary butanol (TBA) was selected as a scavenger for $HO^{\bullet}$. As shown in Figure 5a, when TBA and methanol were introduced, the degradation efficiency of aniline declined by up to 61.7% and 72.9%, respectively, with k-values 0.070 and 0.11 times that of the original. This suggested that the main radical in the electrochemical system was $HO^{\bullet}$ with a portion of $SO_4^{\bullet-}$.[41] The contributions of the different radicals were calculated from the rate constants obtained (Figure 5b), with $HO^{\bullet}$ showing the highest contribution of 87.6% and $SO_4^{\bullet-}$ showing only 5.2%. The presence of these radicals was also verified by EPR. As displayed in Figure 5c, when the

Downloaded from pubs.acs.org/aewcaa/article-pdf/4/10/4625/4093023/ew4c00679.pdf by DOKUZ EYLUL UNIV user on 28 August 2026

https://doi.org/10.1021/acsestwater.4c00679
ACS EST Water 2024, 4, 4625−4635

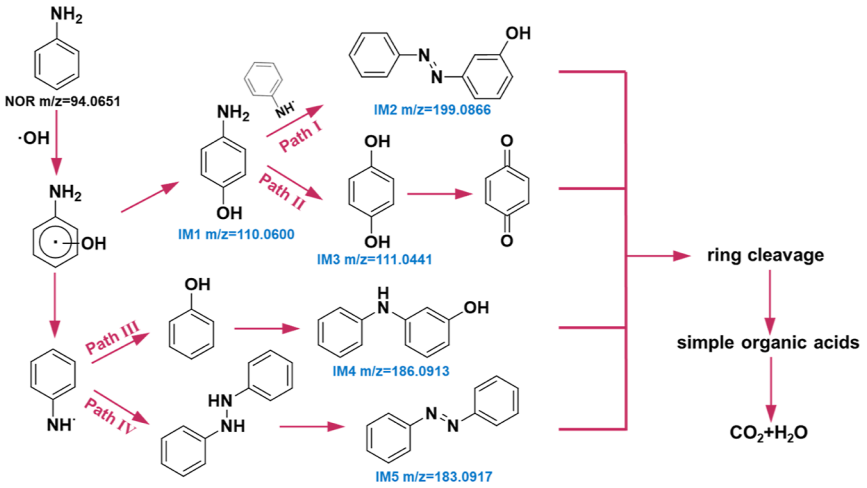


Figure 7. Proposed degradation pathways of aniline in the Fe-CNF-8/EF process.

reaction was carried out for 30 min, a four-line characteristic DMPO-HO$^{\bullet}$ signal with an intensity ratio of 1:2:2:1 could be observed. The weaker DMPO−$SO_4^{\bullet-}$ signal was also detected. The existence of $SO_4^{\bullet-}$ may be explained by the reaction of the background electrolyte SO_4^{2-} with HO$^{\bullet}$. In contrast, the signal intensity of DMPO-HO$^{\bullet}$ in the conventional immersed system was significantly weaker than that of the flow-through system, which is in accordance with the previous results of the HO$^{\bullet}$ concentration detection.

CFD Simulation Study. The degradation performance of contaminants was intimately related to the fluid flow and mass transfer behavior in the designed electrochemical reactor. CFD is an effective tool to characterize electrode properties and fluid conditions.[42] Here, to provide a visual approach to verify the enhancement of mass transfer during the reaction process by flow-through reactors, the concentration of Fe^{2+} (Figure 6a1,b1) and HO$^{\bullet}$ (Figure 6a2,b2) and fluid trajectory distributions (Figure 6a3,b3) in conventional immersed and flow-through EF reactors were investigated by CFD simulations to validate the previous experimental results.

As shown in Figure 6, the concentrations of Fe^{2+} and HO$^{\bullet}$ in the immersed system were more concentrated near the electrode surface, and the concentration drastically decreased as the distance from the electrode surface became larger. Obviously, in the flow-through system, Fe^{2+} and HO$^{\bullet}$ were not only distributed centrally on the electrode surface but had higher concentrations throughout the system due to the forced mass transfer. Moreover, the highest concentration of HO$^{\bullet}$ in the flow-through system was 6.97 μM, which was an increase of about 449% compared to the immersion mode (1.27 μM).

The conventional immersed system possessed a relatively slow velocity with the fastest of 1.24 mm s^{-1}, while the edges occupied a relatively high velocity. Nevertheless, in the flow-through system, the maximum velocity reached as high as 2.22 mm s^{-1}, about twice that of the immersed mode, and the maximum was reached at contact with the nanomaterials (at the jagged bumps in Figure 6b3). The flow velocity distribution of carbon nanofibers without doped nanomaterials in the flow-through system was also simulated (Figure S17), and the maximum flow velocity was 1.71 mm s^{-1}, which was larger than that of the submerged one but still not as fast as that after doping with nanomaterials. More sharp structures in an object have stronger forces and the physical action induced by them is more significant, which is known as the tip effect.[43]

As the SEM results indicated, the surface of the fibers became rough after doping with Fe-MOFs and had dense sharp projections, which made the tip effect more prominent, which enabled the local flow velocity to be enhanced and could assist the reactive material transport.[44] Meanwhile, the Fenton catalytic efficiency could be strongly enhanced in the region with the tip area as the center of high catalytic activity. All of the experimental and simulation data indicated that Fe-CNFs exhibited excellent electrochemical performance and superior flow kinetic behavior in terms of degradation efficiency and mass transfer in flow-through configuration.

Determination of Intermediates. Based on LC−MS, we characterized the oxidation intermediates of aniline in an electrochemical system. Five main products were detected for the degradation of aniline, and the results are shown in Figure 8 and Table S5. Four possible pathways for the degradation of

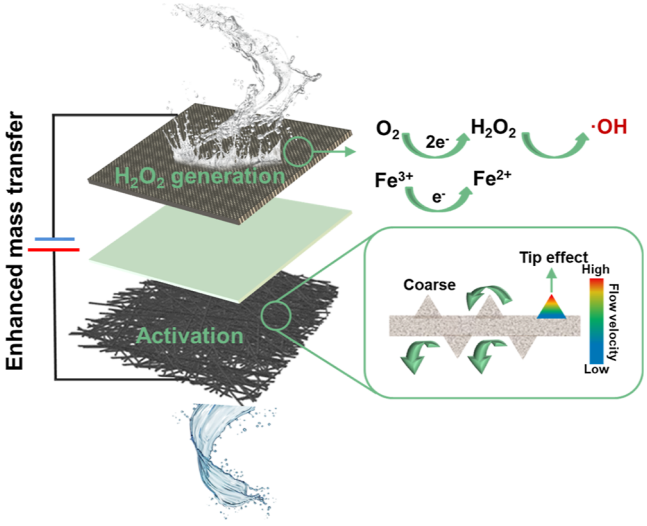


Figure 8. Probable mechanism.

aniline were proposed in conjunction with the main products of aniline degradation reported previously in the literature.[45,46] HO$^{\bullet}$ could form *p*-aminophenol (IM1, m/z = 110.0600) by electrophilic substitution or capture the H atom on the aniline amino group to generate the iminobenzene radical. In pathway I, *p*-hydroxyazobenzene (IM2, m/z = 199.0866) was formed

https://doi.org/10.1021/acsestwater.4c00679
ACS EST Water 2024, 4, 4625−4635

Downloaded from pubs.acs.org/aewcaa/article-pdf/4/10/4625/4093023/ew4c00679.pdf by DOKUZ EYLUL UNIV user on 28 August 2026

by diazotization of the iminobenzene radical with *p*-aminophenol. HO• would further displace the amino group to form hydroquinone (IM3, m/z = 111.0441), which would be further oxidized to *p*-benzoquinone, as shown in path II. In addition, the iminobenzene radical will either polymerize with phenol to form *p*-hydroxydiphenylamine (IM4, m/z = 186.0913) or polymerize its own to form benzidine, which further generates azobenzene (IM5, m/z = 183.0917) as shown in paths III and IV.

There are mainly two different methods of degradation of aniline: polymerization and mineralization. In our study, *p*-benzoquinone and nitrobenzene were not detected, except for polyaniline derivatives. However, depending on the TOC removal result of 40.6%, there should be a ring-opening cleavage process. Although small-molecule organic acids were not detected, based on previous studies, it can be hypothesized that small-molecule organic acids would be present in the final stage of the degradation process.[47] Eventually, the peptide would be further oxidized to CO_2 and H_2O.

Probable Mechanism. According to the above analysis, a probable mechanism for Fe-CNF electrodes in flow-through EF degradation of aniline wastewater is proposed in Figure 7. First, the modified graphite felts reduced dissolved oxygen in solution to H_2O_2 by a 2-electron process (eq 1). Second, under the effect of an electric field, H_2O_2 could interact with the slowly released Fe^{2+} from Fe-CNFs to form hydroxyl radicals in a speedy reaction (eq 2). Fe^{2+} could also be reduced from Fe^{3+} at the cathode, which enabled the Fenton reaction to proceed continuously (eq 3). Meanwhile, the reaction of the more dispersed Fe species in Fe-CNF-8 with H_2O_2 was exacerbated by enhanced mass transfer in the flow-through system, and the slow release of Fe^{2+} was accelerated. Besides, the Fe-CNF-8 nanofibers have a tip effect due to the dense distribution of octahedral nanomaterials, which enhances the local flow rate and contributes to the formation of active species. Subsequently, aniline was polymerized or mineralized to form small-molecule acids, CO_2 and H_2O. Therefore, the rational construction of this EF system enabled the efficient degradation of aniline.

$$O_2 + 2H^+ + 2e^- \rightarrow H_2O_2 \quad (1)$$

$$H_2O_2 + Fe^{2+} + H^+ \rightarrow Fe^{3+} + {}^{\bullet}OH + H_2O \quad (2)$$

$$Fe^{3+} + e^- \rightarrow Fe^{2+} \quad (3)$$

Based on the above analysis, the degradation of aniline was achieved by an enhanced flow-through EF system with a binder-free Fe(II) sustained-release electrode. CFD simulations proved that the flow-through EF system possessed robust ROS generation capability and significantly enhanced the mass transfer process. Furthermore, the flow-through EF system showed good stability and excellent degradation over a wide operating pH range (3−7), highlighting the feasibility of this electrochemical catalytic process for the removal of organic pollutants from wastewater.

CONCLUSIONS

EF technology is currently one of the most promising environmental technologies in wastewater treatment. Its development is mainly limited by the operating pH range, generation of iron sludge, and mass transfer. In this work, a binder-free Fe(II) sustained-release electrode showed excellent performance in a flow-through EF system. Because of the well-dispersed and nanoconfined highly catalytic iron species in the nanofibers, a continuous supply of Fe(II) ions and a controlled homogeneous/heterogeneous coexistence environment benefited a higher removal of aqueous aniline. Meanwhile, the tip effect and the increase in fiber surface roughness improved the chance of water flow making contact with the catalyst, further broadening the pH range of operation (3−7). The results of this study provide new insights into the construction of a rational and efficient EF system to improve the efficiency of pollutant degradation, and they also inspire the exploration and application of iron-based carbonaceous materials in environmental EF for the complete mineralization of wastewater.

ASSOCIATED CONTENT

Data Availability Statement

Data will be made available on request.

Supporting Information

The Supporting Information is available free of charge at https://pubs.acs.org/doi/10.1021/acsestwater.4c00679.

Analytical methods; calculation formula; illustration of the preparation process of Fe-CNFs; schematic diagram of the reactor; SEM images of PAN and CNF-8; SEM and TEM images Fe-CNF-7, Fe-CNF-9, and Fe-CNF-10; Raman and XPS spectra of Fe-CNFs; effect of voltage on H_2O_2 production; effect of initial pH, flow rates, voltage, inorganic ions, and the corresponding pseudo-first-order rate constant of aniline degradation; consecutive runs of Fe-CNF-8 on aniline removal efficiency; SEM images, XRD patterns, XPS spectra, and Fe 2p of used Fe-CNF-8; equivalent circuit diagram; Z' vs the reciprocal of the square root of frequency ($\omega^{-1/2}$) in the intermediate to the low-frequency range; CFD simulations; iron content, surface textural properties, specific capacitance, R_s and R_{ct} of Fe-CNFs; and LC−MS data (PDF)

AUTHOR INFORMATION

Corresponding Authors

Yujun Zhou − *Key Laboratory of Jiangsu Province for Chemical Pollution Control and Resources Reuse, School of Environmental and Biological Engineering, Nanjing University of Science and Technology, Nanjing 210094, China*; Email: yjzhou@njust.edu.cn

Jiansheng Li − *Key Laboratory of Jiangsu Province for Chemical Pollution Control and Resources Reuse, School of Environmental and Biological Engineering, Nanjing University of Science and Technology, Nanjing 210094, China*; orcid.org/0000-0002-3708-3677; Email: lijsh@njust.edu.cn

Authors

Jiamin Gao − *Key Laboratory of Jiangsu Province for Chemical Pollution Control and Resources Reuse, School of Environmental and Biological Engineering, Nanjing University of Science and Technology, Nanjing 210094, China*

Wei Zhang − *Key Laboratory of Drinking Water Science and Technology, Research Center for Eco-Environmental Sciences, Chinese Academy of Sciences, Beijing 100085, China*; orcid.org/0000-0002-9559-2496

Xuran Yang − *Key Laboratory of Jiangsu Province for Chemical Pollution Control and Resources Reuse, School of*

Downloaded from pubs.acs.org/aewcaa/article-pdf/4/10/4625/4093023/ew4c00679.pdf by DOKUZ EYLUL UNIV user on 28 August 2026

https://doi.org/10.1021/acsestwater.4c00679
ACS EST Water 2024, 4, 4625−4635

Environmental and Biological Engineering, Nanjing University of Science and Technology, Nanjing 210094, China

Yiyuan Yao − *Key Laboratory of Jiangsu Province for Chemical Pollution Control and Resources Reuse, School of Environmental and Biological Engineering, Nanjing University of Science and Technology, Nanjing 210094, China*

Chengming Xiao − *Key Laboratory of Jiangsu Province for Chemical Pollution Control and Resources Reuse, School of Environmental and Biological Engineering, Nanjing University of Science and Technology, Nanjing 210094, China*

Xin Guo − *Key Laboratory of Jiangsu Province for Chemical Pollution Control and Resources Reuse, School of Environmental and Biological Engineering, Nanjing University of Science and Technology, Nanjing 210094, China*

Junwen Qi − *Key Laboratory of Jiangsu Province for Chemical Pollution Control and Resources Reuse, School of Environmental and Biological Engineering, Nanjing University of Science and Technology, Nanjing 210094, China;* orcid.org/0000-0001-6587-5797

Zhigao Zhu − *Key Laboratory of Jiangsu Province for Chemical Pollution Control and Resources Reuse, School of Environmental and Biological Engineering, Nanjing University of Science and Technology, Nanjing 210094, China*

Yue Yang − *Key Laboratory of Jiangsu Province for Chemical Pollution Control and Resources Reuse, School of Environmental and Biological Engineering, Nanjing University of Science and Technology, Nanjing 210094, China*

Complete contact information is available at: https://pubs.acs.org/10.1021/acsestwater.4c00679

Author Contributions

Jiamin Gao conceptualization, writing—original draft, diagraph analysis; **Yujun Zhou** writing—original draft, formal analysis, investigation; **Wei Zhang** validation, methodology; **Xuran Yang** methodology, formal analysis; **Yiyuan Yao** software, data curation; **Junwen Qi** Discussion on BET analysis; **Zhigao Zhu** visualization, resources; **Yue Yang** investigation, methodology; **Jiansheng Li** conceptualization, project management and hosting, supervision, writing—review and editing.

Notes

The authors declare no competing financial interest.

■ ACKNOWLEDGMENTS

This work was supported by the National Natural Science Foundation of China (52200098) and Jiangsu Agriculture Science and Technology Innovation Fund (CX(22)3135).

■ REFERENCES

(1) Hu, J.; Wang, S.; Yu, J.; Nie, W.; Sun, J.; Wang, S. Duet Fe_3C and FeN_x Sites for H_2O_2 Generation and Activation toward Enhanced Electro-Fenton Performance in Wastewater Treatment. *Environ. Sci. Technol.* **2021**, *55* (2), 1260−1269.

(2) Zhou, Y.; Ji, Q.; Liu, H.; Qu, J. Pore Structure-Dependent Mass Transport in Flow-through Electrodes for Water Remediation. *Environ. Sci. Technol.* **2018**, *52* (13), 7477−7485.

(3) Jiang, W.-L.; Xia, X.; Han, J.-L.; Ding, Y.-C.; Haider, M. R.; Wang, A.-J. Graphene Modified Electro-Fenton Catalytic Membrane for in Situ Degradation of Antibiotic Florfenicol. *Environ. Sci. Technol.* **2018**, *52* (17), 9972−9982.

(4) Yi, J.; Al-Dhabi, N. A.; Hu, T.; Soyol-Erdene, T.-O.; Bayanjargal, O.; Liu, E.; Tang, W. Highly efficient degradation of antibiotic metronidazole by an environmental-friendly metal-free dual-cathode electro-Fenton system. *Chem. Eng. J.* **2024**, *492*, 152447.

(5) Zhang, J.; Wang, D.; Zhao, F.; Feng, J.; Feng, H.; Luo, J.; Tang, W. Ferrate modified carbon felt as excellent heterogeneous electro-Fenton cathode for chloramphenicol degradation. *Water Res.* **2022**, *227*, 119324.

(6) Guo, D.; Liu, Y.; Ji, H.; Wang, C.-C.; Chen, B.; Shen, C.; Li, F.; Wang, Y.; Lu, P.; Liu, W. Silicate-Enhanced Heterogeneous Flow-Through Electro-Fenton System Using Iron Oxides under Nano-confinement. *Environ. Sci. Technol.* **2021**, *55* (6), 4045−4053.

(7) Liu, F.; Liu, Y.; Yao, Q.; Wang, Y.; Fang, X.; Shen, C.; Li, F.; Huang, M.; Wang, Z.; Sand, W.; Xie, J. Supported Atomically-Precise Gold Nanoclusters for Enhanced Flow-through Electro-Fenton. *Environ. Sci. Technol.* **2020**, *54* (9), 5913−5921.

(8) Ding, J.; Tang, Y.; Zheng, S.; Zhang, S.; Xue, H.; Kong, Q.; Pang, H. The synthesis of MOF derived carbon and its application in water treatment. *Nano Res.* **2022**, *15* (8), 6793−6818.

(9) Hu, T.; Tang, L.; Feng, H.; Zhang, J.; Li, X.; Zuo, Y.; Lu, Z.; Tang, W. Metal-organic frameworks (MOFs) and their derivatives as emerging catalysts for electro-Fenton process in water purification. *Coord. Chem. Rev.* **2022**, *451*, 214277.

(10) Gao, S.; Fan, B.; Feng, R.; Ye, C.; Wei, X.; Liu, J.; Bu, X. N-doped-carbon-coated Fe3O4 from metal-organic framework as efficient electrocatalyst for ORR. *Nano Energy* **2017**, *40*, 462−470.

(11) Liu, E.; Hu, T.; Al-Dhabi, N. A.; Soyol-Erdene, T.-O.; Bayanjargal, O.; Zuo, Y.; Wang, J.; Tang, W. MOF-derived Fe/Ni@C marigold-like nanosheets as heterogeneous electro-Fenton cathode for efficient antibiotic oxytetracycline degradation. *Environ. Res.* **2024**, *247*, 118357.

(12) Zhao, K.; Quan, X.; Su, Y.; Qin, X.; Chen, S.; Yu, H. Enhanced Chlorinated Pollutant Degradation by the Synergistic Effect between Dechlorination and Hydroxyl Radical Oxidation on a Bimetallic Single-Atom Catalyst. *Environ. Sci. Technol.* **2021**, *55* (20), 14194−14203.

(13) Wang, C.; Cheng, P.; Yao, Y.; Yamauchi, Y.; Yan, X.; Li, J.; Na, J. In-situ fabrication of nanoarchitectured MOF filter for water purification. *J. Hazard. Mater.* **2020**, *392*, 122164.

(14) Liu, Y.; Li, J.; Zhou, B.; Bai, J.; Zheng, Q.; Zhang, J.; Cai, W. Comparison of photoelectrochemical properties of TiO_2-nanotube-array photoanode prepared by anodization in different electrolyte. *Environ. Chem. Lett.* **2009**, *7* (4), 363−368.

(15) Guo, D.; Yao, Y.; You, S.; Jin, L.; Lu, P.; Liu, Y. Ultrafast degradation of micropollutants in water via electro-periodate activation catalyzed by nanoconfined Fe2O3. *Appl. Catal., B* **2022**, *309*, 121289.

(16) Wang, L.; Liu, Z.; Wang, Z.; Ma, Q.; Guo, Z.; Shen, G.; Wang, K.; Xu, X.; Liu, Y.; Yuan, X. Up-shifting the desalination rate limit of capacitive deionization via integrating chloride-capturing Bi nanocluster with flow-through cell architecture. *Chem. Eng. J.* **2023**, *460*, 141726.

(17) Feng, A.; Feng, J.; Xing, W.; Jiang, K.; Tang, W. Versatile applications of electrochemical flow-through systems in water treatment processes. *Chem. Eng. J.* **2023**, *473*, 145400.

(18) Chen, Y.; Zhang, G.; Ji, Q.; Lan, H.; Liu, H.; Qu, J. Visualization of Electrochemically Accessible Sites in Flow-through Mode for Maximizing Available Active Area toward Superior Electrocatalytic Ammonia Oxidation. *Environ. Sci. Technol.* **2022**, *56* (13), 9722−9731.

(19) Yang, W.; Wang, Y. Enhanced electron and mass transfer flow-through cell with C3N4-MoS2 supported on three-dimensional graphene photoanode for the removal of antibiotic and antibacterial potencies in ampicillin wastewater. *Appl. Catal., B* **2021**, *282*, 119574.

Downloaded from pubs.acs.org/aewcaa/article-pdf/4/10/4625/4093023/ew4c00679.pdf by DOKUZ EYLUL UNIV user on 28 August 2026

(20) García-Espinoza, J. D.; Robles, I.; Durán-Moreno, A.; Godínez, L. A. Study of the performance of a cylindrical flow-through electro-Fenton reactor using different arrangements of carbon felt electrodes: effect of key operating parameters. *Environ. Sci. Pollut. Res.* **2022**, *29* (28), 42305−42318.
(21) Sun, M.; Wang, X.; Winter, L. R.; Zhao, Y.; Ma, W.; Hedtke, T.; Kim, J.-H.; Elimelech, M. Electrified Membranes for Water Treatment Applications. *ACS ES&T Eng.* **2021**, *1* (4), 725−752.
(22) Zeng, T.; Yu, M.; Zhang, H.; He, Z.; Chen, J.; Song, S. Fe/Fe3C@N-doped porous carbon hybrids derived from nano-scale MOFs: robust and enhanced heterogeneous catalyst for peroxymonosulfate activation. *Catal. Sci. Technol.* **2017**, *7* (2), 396−404.
(23) Du, X.; Fu, W.; Su, P.; Cai, J.; Zhou, M. Internal-micro-electrolysis-enhanced heterogeneous electro-Fenton process catalyzed by Fe/Fe_3C@PC core−shell hybrid for sulfamethazine degradation. *Chem. Eng. J.* **2020**, *398*, 125681.
(24) Férey, G.; Mellot-Draznieks, C.; Serre, C.; Millange, F.; Dutour, J.; Surblé, S.; Margiolaki, I. A Chromium Terephthalate−BasedSolid with Unusually Large PoreVolumes and Surface Area. *Science* **2005**, *309* (5743), 2040−2042.
(25) Zhang, Y.; Liu, F.; Yang, Z.; Qian, J.; Pan, B. Weakly hydrophobic nanoconfinement by graphene aerogels greatly enhances the reactivity and ambient stability of reactivity of MIL-101-Fe in Fenton-like reaction. *Nano Res.* **2020**, *14* (7), 2383−2389.
(26) Doan, V.-D.; Huynh, B.-A.; Pham, H. A. L.; Vasseghian, Y.; Le, V. T. Cu_2O/Fe_3O_4/MIL-101(Fe) nanocomposite as a highly efficient and recyclable visible-light-driven catalyst for degradation of ciprofloxacin. *Environ. Res.* **2021**, *201*, 111593.
(27) Yang, D.; Zhang, L.; Wang, N.; Yu, T.; Sun, W.; Luo, N.; Feng, Y.; Liu, W.; Wang, D. Humidity-Resistant Triboelectric Nanogenerator Based on a Swelling-Resistant and Antiwear PAN/PVA-$CaCl_2$ Composite Film for Seawater Desalination. *Adv. Funct. Mater.* **2023**, *34* (2), 2306702.
(28) Zhang, M.; Luo, R.; Wang, C.; Zhang, W.; Yan, X.; Sun, X.; Wang, L.; Li, J. Confined pyrolysis of metal−organic frameworks to N-doped hierarchical carbon for non-radical dominated advanced oxidation processes. *J. Mater. Chem. A* **2019**, *7* (20), 12547−12555.
(29) Chen, S.; Li, M.; Zhang, M.; Wang, C.; Luo, R.; Yan, X.; Zhang, H.; Qi, J.; Sun, X.; Li, J. Metal organic framework derived one-dimensional porous Fe/N-doped carbon nanofibers with enhanced catalytic performance. *J. Hazard. Mater.* **2021**, *416*, 126101.
(30) Fang, R.; Lu, C.; Zhong, Y.; Xiao, Z.; Liang, C.; Huang, H.; Gan, Y.; Zhang, J.; Pan, G.; Xia, X.; Xia, Y.; Zhang, W. Puffed Rice Carbon with Coupled Sulfur and Metal Iron for High-Efficiency Mercury Removal in Aqueous Solution. *Environ. Sci. Technol.* **2020**, *54* (4), 2539−2547.
(31) Shen, W.; Kou, W.; Liu, Y.; Dai, Y.; Zheng, W.; He, G.; Wang, S.; Zhang, Y.; Wu, X.; Fan, S.; Li, X. Fe3C-doped asymmetric porous carbon membrane binder-free integrated materials as high performance anodes of lithium-ion batteries. *Chem. Eng. J.* **2019**, *368*, 310−320.
(32) Gang, H.; Deng, H.; Yan, L.; Wu, B.; Alhassan, S. I.; Cao, Y.; Wei, D.; Wang, H. Surface redox pseudocapacitance boosting Fe/Fe3C nanoparticles-encapsulated N-doped graphene-like carbon for high-performance capacitive deionization. *J. Colloid Interface Sci.* **2023**, *638*, 252−262.
(33) Fan, M.; Wang, Z.; Sun, K.; Wang, A.; Zhao, Y.; Yuan, Q.; Wang, R.; Raj, J.; Wu, J.; Jiang, J.; Wang, L. N-B-OH Site-Activated Graphene Quantum Dots for Boosting Electrochemical Hydrogen Peroxide Production. *Adv. Mater.* **2023**, *35* (17), 2209086.
(34) Wu, J.-C.; Chuang, Y.-H.; Liou, S. Y. H.; Li, Q.; Hou, C.-H. In situ engineering of highly conductive TiO2/carbon heterostructure fibers for enhanced electrocatalytic degradation of water pollutants. *J. Hazard. Mater.* **2022**, *429*, 128328.
(35) Liu, Y.; Liu, F.; Qi, Z.; Shen, C.; Li, F.; Ma, C.; Huang, M.; Wang, Z.; Li, J. Simultaneous oxidation and sorption of highly toxic Sb(III) using a dual-functional electroactive filter. *Environ. Pollut.* **2019**, *251*, 72−80.
(36) Su, P.; Du, X.; Zheng, Y.; Fu, W.; Zhang, Q.; Zhou, M. Interface-confined multi-layered reaction centers between Ce-MOFs and Fe3O4@C for heterogeneous electro-Fenton at wide pH 3−9: Mediation of Ce^{3+}/Ce^{4+} and oxygen vacancy. *Chem. Eng. J.* **2022**, *433*, 133597.
(37) Shi, L.; Shi, Y.; Zhuo, S.; Zhang, C.; Aldrees, Y.; Aleid, S.; Wang, P. Multi-functional 3D honeycomb ceramic plate for clean water production by heterogeneous photo-Fenton reaction and solar-driven water evaporation. *Nano Energy* **2019**, *60*, 222−230.
(38) Zhang, Y.; Xu, X.; Pan, Y.; Xu, L.; Zhou, M. Pre-magnetized Fe0 activated persulphate for the degradation of nitrobenzene in groundwater. *Sep. Purif. Technol.* **2019**, *212*, 555−562.
(39) Tian, Y.; Zhou, M.; Pan, Y.; Du, X.; Wang, Q. MoS_2 as highly efficient co-catalyst enhancing the performance of Fe0 based electro-Fenton process in degradation of sulfamethazine: Approach and mechanism. *Chem. Eng. J.* **2021**, *403*, 126361.
(40) Wang, C.; Zheng, T.; Luo, R.; Liu, C.; Zhang, M.; Li, J.; Sun, X.; Shen, J.; Han, W.; Wang, L. In Situ Growth of ZIF-8 on PAN Fibrous Filters for Highly Efficient U(VI) Removal. *ACS Appl. Mater. Interfaces* **2018**, *10* (28), 24164−24171.
(41) Wang, C.; Wang, H.; Na, J.; Yao, Y.; Azhar, A.; Yan, X.; Qi, J.; Yamauchi, Y.; Li, J. 0D−1D hybrid nanoarchitectonics: tailored design of FeCo@N−C yolk−shell nanoreactors with dual sites for excellent Fenton-like catalysis. *Chem. Sci.* **2021**, *12* (46), 15418−15422.
(42) Huo, Z.-Y.; Du, Y.; Chen, Z.; Wu, Y.-H.; Hu, H.-Y. Evaluation and prospects of nanomaterial-enabled innovative processes and devices for water disinfection: A state-of-the-art review. *Water Res.* **2020**, *173*, 115581.
(43) Liu, W.; Li, X.; Wang, Y.; Yang, D.; Guo, Z.; Liu, M.; Wang, J. Multi-branched AgAuPt nanoparticles for efficient electrocatalytic hydrogen evolution: Synergism of tip-enhanced electric field effect and local electric field effect. *J. Energy Chem.* **2023**, *81*, 339−348.
(44) Liu, P.; Chen, B.; Liang, C.; Yao, W.; Cui, Y.; Hu, S.; Zou, P.; Zhang, H.; Fan, H. J.; Yang, C. Tip-Enhanced Electric Field: A New Mechanism Promoting Mass Transfer in Oxygen Evolution Reactions. *Adv. Mater.* **2021**, *33* (9), 2007377.
(45) Benito, A.; Penadés, A.; Lliberia, J. L.; Gonzalez-Olmos, R. Degradation pathways of aniline in aqueous solutions during electro-oxidation with BDD electrodes and UV/H_2O_2 treatment. *Chemosphere* **2017**, *166*, 230−237.
(46) Zhu, J.; Chen, C.; Li, Y.; Zhou, L.; Lan, Y. Rapid degradation of aniline by peroxydisulfate activated with copper-nickel binary oxysulfide. *Sep. Purif. Technol.* **2019**, *209*, 1007−1015.
(47) Liu, Y.; Zhang, H.; Sun, J.; Liu, J.; Shen, X.; Zhan, J.; Zhang, A.; Ognier, S.; Cavadias, S.; Li, P. Degradation of aniline in aqueous solution using non-thermal plasma generated in microbubbles. *Chem. Eng. J.* **2018**, *345*, 679−687.

Downloaded from pubs.acs.org/aewcaa/article-pdf/4/10/4625/4093023/ew4c00679.pdf by DOKUZ EYLUL UNIV user on 28 August 2026

https://doi.org/10.1021/acsestwater.4c00679
ACS EST Water 2024, 4, 4625−4635